



Supplementary Materials for

Architecture of the nuclear pore complex coat

Tobias Stuwe, Ana R. Correia, Daniel H. Lin, Marcin Paduch, Vincent T. Lu, Anthony A. Kossiakoff, and André Hoelz

correspondence to: hoelz@caltech.edu

This PDF file includes:

Materials and Methods
Figs. S1 to S13
Tables S1 to S2
Captions for Movies S1 to S4

Other Supplementary Materials for this manuscript includes the following:

Movies S1 to S4

Materials and Methods

Protein expression and purification. DNA fragments encoding full-length Sec13, Nup145C (residues 75-712), full-length Seh1, and Nup85 (44-744) were PCR amplified and cloned as pairs into the pET-Duet1 expression vector (Novagen). Nup145C and Nup85 were cloned into the first multiple cloning site using BamHI and NotI restriction sites, whereas Sec13 and Seh1 were cloned into the second multiple cloning site using NdeI and XhoI restriction sites. Nup84 (residues 1-451) was cloned into a modified pET28a vector, which contains an N-terminal hexahistidine tag followed by a PreScission protease cleavage site, using NdeI and NotI restriction sites (18). The expression construct for Nup120 was described previously (2). The selected synthetic antibody (sAB) fragments of sAB-57 and sAB-87 were cloned into the pSFV4 vector (Peter Loppnau, Structural Genomics Consortium, University of Toronto) using the restriction sites NcoI and SallI, and subsequently digested using SallI and BsaI and religated to obtain the C-terminal hexahistidine tag. The details of the bacterial expression constructs are listed in [table S1](#).

All proteins were expressed in *Escherichia coli* BL21-Codon-Plus (DE3)-RIL cells (Stratagene) in Luria-Bertani media. Seleno-L-methionine-labeled (SeMet) Sec13•Nup145C, Seh1•Nup85, and Nup84^{NTD} were produced in a synthetic medium that suppresses methionine biosynthesis, following standard protocols. For all nucleoporins, expression was induced at an OD600 of 0.8 with 0.5 mM isopropyl- β -D-thiogalactopyranoside (IPTG), followed by growth at 18 °C for 18 hours. Cells were harvested by centrifugation and resuspended in a buffer containing 20 mM TRIS (pH 8.0), 500 mM NaCl, 20 mM imidazole, 4 mM β -mercaptoethanol (β -ME), and complete EDTA-free protease inhibitor mixture (Roche).

For purification, cells were lysed with a cell disruptor (Avestin) and DNase I (Roche) was added to the lysate before centrifugation at 30,000 \times g for 1 hour. The supernatant was filtered through a 0.45- μ m filter (Millipore) and loaded onto a nickel-nitrilotriacetic acid (Ni-NTA) column (Qiagen) equilibrated in 20 mM TRIS (pH 8.0), 500 mM NaCl, 20 mM imidazole, and 4 mM β -ME. Protein was eluted with a linear gradient of 20 mM TRIS (pH 8.0), 500 mM NaCl, 500 mM imidazole, and 4 mM β -ME. Protein-containing fractions were pooled, incubated with either PreScission (GE Healthcare) or ULP1 protease, and dialyzed overnight at 4 °C against a buffer containing 20 mM TRIS (pH 8.0), 100 mM NaCl, and 5 mM DTT. Next the protein was loaded onto a Mono Q 10/100 GL ion-exchange column (GE Healthcare) equilibrated in a buffer containing 20 mM TRIS (pH 8.0), 100 mM NaCl, and 5 mM DTT and eluted using a NaCl gradient. Protein-containing fractions were concentrated in a centrifugal filter (Millipore) and loaded onto a HiLoad Superdex 200 16/60 gel filtration column (GE Healthcare) equilibrated in a buffer containing 20 mM TRIS (pH 8.0), 100 mM NaCl, and 5 mM DTT. Protein-containing fractions were pooled and concentrated to 20 mg/mL for biochemical interaction experiments and CNC reconstitution.

sABs were expressed, harvested, and lysed in a similar fashion, but the cells were induced at an OD600 of 0.9 with 0.25 mM IPTG and grown at 25 °C for 18 hours. After lysis, the lysate was incubated at 65 °C for 30 minutes and then cooled on ice for 15 minutes before centrifugation. Protein-containing fractions from the Ni-NTA affinity purification were pooled and loaded onto a 5 mL HiTrap MabSelect SuRe column (GE

Healthcare) equilibrated in a buffer containing 20 mM TRIS (pH 8.0), 500 mM NaCl, 20 mM imidazole, and 4 mM β -ME. The protein was eluted using a linear gradient of an elution buffer, containing 0.1 M sodium citrate (pH 3.2). To rapidly increase the pH after elution, the fractions were collected into tubes containing 200 μ l of 1 M TRIS (pH 9.0). The eluted fractions were dialysed against a buffer containing 20 mM TRIS (pH 8.0) and 100 mM NaCl and concentrated to 10 mg/ml for biochemical interaction experiments and crystallization.

Reconstitution of CNC complexes. Seh1•Nup85•Nup120 (Trimer1) was purified by co-lysis of cells expressing Seh1•Nup85 or Nup120, following the protocol described above. For the reconstitution of Sec13•Nup145C•Nup84^{NTD} (Trimer2), purified Sec13•Nup145C was mixed with a 1.2 fold molar excess of Nup84^{NTD}, incubated on ice for 30 minutes, and loaded onto a HiLoad Superdex 200 16/60 gel filtration column equilibrated in a buffer containing 20 mM TRIS (pH 8.0), 100 mM NaCl, and 5 mM DTT. Trimer1 and Trimer2 containing fractions were pooled, concentrated, mixed with a 1.2 molar excess of Trimer2, incubated on ice for 1 hour, and injected onto a HiLoad Superdex 200 16/60 gel filtration column equilibrated in the same buffer. Fractions containing the reconstituted CNC were pooled and concentrated to 10 mg/ml for sAB interaction experiments. For SeMet labeled CNC, SeMet-labeled Seh1•Nup85, Sec13•Nup145C, and Nup84^{NTD} were purified and used instead of the native proteins. SeMet labeling of Nup120 rendered the protein insoluble in our bacterial expression system and thus native Nup120 was used for the reconstitution of the SeMet-labeled CNC. For the generation of CNC•sAB complexes, native or SeMet-labeled CNC were mixed with 1.5 fold molar excess of sAB-57 or a 1:1 mixture of sAB-57 and sAB-87 and loaded onto a HiLoad Superdex 200 16/60 gel filtration column (GE Healthcare) equilibrated in a buffer containing 20 mM TRIS (pH 8.0), 100 mM NaCl, and 5 mM DTT. DTT was included in the buffer as it was necessary for CNC stability and had no effect on the integrity of the sABs. Fractions containing the various CNC complexes were pooled and concentrated to 10 mg/mL for crystallization.

sAB selection and characterization. The generation and screening of conformation-specific sABs has been described previously (5). Briefly, a modified yeast CNC was reconstituted with a Nup84^{NTD} variant that harbored an N-terminal avi-tag. The complex was biotinylated in a 2 mL reaction by incubating 40 μ M protein with a buffer containing 50 mM BICINE (pH 8.3), 100 mM biotin, 10 mM ATP, 10 mM magnesium acetate, and 30 μ g biotin ligase (BirA) at 30 °C for 2 hours. After labeling, protein was buffer exchanged using a 5 mL HiTrap Desalting column (GE Healthcare) equilibrated with a buffer containing 20 mM TRIS (pH 8.0), 100 mM NaCl, and 5 mM DTT and purified again using a HiLoad Superdex 200 16/60 gel filtration column equilibrated in the same buffer. The extent of Nup84^{NTD} biotinylation and efficiency of capture were tested by incubating 25 μ g of protein with 50 μ L of Streptavidin MagneSphere particles (Thermo Scientific), washing once with 50 μ L of a buffer containing 20 mM TRIS (pH 8.0), 100 mM NaCl, and 5 mM DTT, and resolving the bound proteins on a SDS-PAGE gel. Four rounds of competitive selection were performed using 100 nM (round 1), 50 nM (round 2), 10 nM (round 3), and 10 nM (round 4) biotinylated protein target and a phage display library according to previously published protocols (5). In case of sAB-57 biotinylated

yeast CNC was used and to eliminate sABs that recognized unassociated CNC components, 1 μM of non-biotinylated CNC subunits (Seh1•Nup85, Nup120^{NTD}, Sec13•Nup145C, and Nup84^{NTD}) were used as competitors in all solutions during the last three rounds of selection. Phages were preincubated with competitors for 1 hour at room temperature. sAB-87 was obtained in a selection where biotinylated Nup120^{NTD} was used and no competition was performed. After successful selection, the specificity of candidate sABs was tested against the assembled biotinylated yeast CNC, as well as individual biotinylated subunits using a single point competitive ELISA assay (5). Only sequence-unique sABs with the desired binding properties were nominated for further biochemical characterization. To evaluate the binding affinity and specificity of the selected sABs, 1.5-fold molar excess of sAB was incubated with the reconstituted CNC or individual CNC components and loaded onto a MonoQ 5/50 GL ion-exchange column (GE Healthcare) equilibrated in a buffer containing 20 mM TRIS (pH 8.0), 100 mM NaCl, and 5 mM DTT and eluted using a NaCl gradient. Interacting sABs eluted with the CNC components, whereas non-interacting sABs eluted prior to the gradient step. Initially, only sABs that specifically interacted with the fully assembled CNC were systematically tested in crystallization trials. To improve the diffraction properties of the CNC•sAB-57 crystals, additional sABs with the ability to bind individual CNC components were systematically screened for crystal formation. The addition of sAB-87 to the CNC•sAB-57 complex yielded a new crystal form with distinct packing and different space group.

Protein crystallization, heavy metal derivatization and data collection. Protein crystallization was carried out at 21 °C in hanging drops consisting of 1.0 μL protein solution (2 mg/ml) and 1.0 μL reservoir solution. Crystals appeared in the monoclinic space group C2 with one copy of the CNC•sAB-57 complex in the asymmetric unit. The crystals were improved by microseeding, which resulted in crystals that grew as thin plates with maximum dimensions of $\sim 30 \times 300 \times 300 \mu\text{m}^3$ within 1 week. Crystals used for diffraction experiments were grown in 0.1 M MES, pH 6.7, 5 % (w/v) PEG 20000, and 3% (v/v) ethanol. Crystals were cryoprotected by gradually supplementing the drop with 36 % (v/v) ethylene glycol (in 1 % steps, every 5 minutes) and flash frozen in liquid nitrogen. Crystals of the CNC changed morphology after the inclusion of a second sAB (sAB-87) and appeared in the orthorhombic space group P2₁2₁2₁ with one copy of the CNC•sAB-57•sAB-87 complex in the asymmetric unit. Crystals grew to maximum dimensions of $\sim 50 \times 100 \times 150 \mu\text{m}^3$ within 1 week. Crystals used for diffraction experiments were grown in 0.1 M MES, pH 6.5, 5 % (w/v) PEG 20000, and 20 mM SrCl₂. Crystals were cryoprotected by serial transfers into solutions containing 5 %, 10 %, 15 %, 20 % and 25 % (v/v) ethylene glycol supplemented reservoir solution. This crystal form typically diffracted to a resolution limit of $\sim 9 \text{ \AA}$. During a systematic heavy metal derivative screen individual SeMet labeled crystals were identified that yielded X-ray diffraction data to a resolution limit of 7.6 \AA after soaking with 1 mM potassium hexachloroosmate (K₂OsCl₆). Native crystals were derivatized by adding 0.2 μL of a saturated tantalum bromide cluster (Ta₆Br₁₄) solution to the crystallization drop and incubated for 1 week. X-ray diffraction data were collected at 100 K at beamline BL12-2 at the Stanford Synchrotron Radiation Source (SSRL) and beamline GM/CA-CAT 23ID-

D at the Advanced Photon Source (APS) on a Pilatus3 detector. Thousands of CNC crystals were screened to yield the reported X-ray diffraction datasets.

Structure determination and model building. X-ray diffraction data was processed with XDS (19). The structures for both crystal forms were solved by iterative cycles of molecular replacement (MR) using Phaser (20).

For structure determination of the first crystal form containing the CNC•sAB-57 complex in the space group C2, Phaser was run with the assumption that the asymmetric unit (ASU) harbored one CNC•sAB-57 complex (~450 kDa), corresponding to a solvent content of ~83 %. The crystal structures of the *S. cerevisiae* CNC components Sec13•Nup145C^{NTD} (PDB ID 3IKO) Seh1•Nup85^{NTD} (PDB ID 3F3F), Nup120^{NTD} (PDB ID 3F7F), Nup84^{NTD} (PDB ID 3IKO), and a structure of the sAB scaffold (PDB ID 3PGF) were used sequentially as search models with a model variance of 100 % sequence identity (6-10). MR was performed in the above search order and the top solutions were taken from each MR search to look for the next molecule. During each MR round, Phaser robustly obtained solutions with clear separation from other solutions after the packing test with Log Likelihood Gain (LLG) values and refined translation function Z-scores (TFZ) of: (1) LLG=43, TFZ=9.0 (Sec13•Nup145C^{NTD}), (2) LLG=94, TFZ=11.6 (Seh1•Nup85^{NTD}), (3) LLG=190, TFZ=6.9 (Nup120^{NTD}), (4) LLG=202, TFZ=8.1 (Nup84^{NTD}), and (5) LLG=310, TFZ=8.5 (sAB scaffold) (fig. S1A, B).

The correctness of the final solution output from Phaser was assessed on the following criteria: (1) clear separation of the best scoring solutions from the remaining solutions at every step, (2) very high TFZ scores after each step, as TFZ scores above 8 usually indicate a definite solution, (3) increasing LLG scores at each step indicating that each additional molecule was improving the solution, (4) an internal test that the Nup84^{NTD} was placed in the same orientation as previously determined in the Sec13•Nup145C•Nup84^{NTD} crystal structure (8), despite no *a priori* information restricting it to that location, (5) the overall shape of the solution was consistent with low resolution EM reconstructions, and most importantly (6) the appearance of strong additional features in the calculated electron density maps of the final solution. Strong positive difference density for the helices of the triskelion were clearly visible in the |Fo|-|Fc| map output from PHENIX (fig. S2A). Density modification of the MR solution using RESOLVE (21) yielded an improved electron density map with additional density for loops connecting the new helices despite no additional model building (fig. S2A). Furthermore, no additional density was observed in the solvent channels (fig. S4A). Model building was performed with COOT (22). The α -helical C-terminal domains of Nup145C, Nup85, and Nup120 formed distinctive arrays of tubular electron density at 7.4 Å, into which we were able to place idealized α -helices. As the C-terminal domains of Nup145C, Nup85, and Nup120 are connected to their respective N-terminal domains by short loops, a preliminary model for the connectivity and directionality of the helices was traced starting from the C-terminus of each previously determined structure. This preliminary model was validated by comparison with the helical arrangement in the *S. pombe* homolog of Nup120, which could be structurally aligned with the helices assigned to the C-terminal domain of Nup120. Once all of the helices were successfully assigned to each protein, the connectivity of all three proteins could be assigned with the aid of the helix and loop lengths from a secondary structure prediction (fig. S3D). As the electron

density does not possess features to assign the sequence register, the numbering in the structure is approximate and only reflects the order and directionality of each helix and thus we modeled the triskelion with the sidechains truncated at the C β position.

For structure determination of the second crystal form, containing the CNC•sAB-57•sAB-87 complex, which grew in the space group P2₁2₁2₁, sequential Phaser searches for the Sec13•Nup145C^{NTD}•Nup84^{NTD} heterotrimer (PDB ID 3IKO), Nup120^{NTD} (PDB ID 3F7F), and the sAB scaffold structure (PDB ID 3PGF) produced clearly separated solutions with the following scores: (1) LLG=239, TFZ=13.3 (Sec13•Nup145C^{NTD}•Nup84^{NTD}), (2) LLG=653, TFZ=12.2 (Nup120^{NTD}), and (3) LLG=887, TFZ=11.2 (sAB scaffold, sAB-87) (fig. S1C, D). Despite exhaustive attempts with both the normal Phaser pipeline and brute-force translation and rotation searches, no MR solutions were identified for Seh1•Nup85^{NTD} (PDB ID 3F3F) and a second sAB scaffold (PDB ID 3PGF) for sAB-57 and these molecules are likely disordered in the crystal. The resulting maps were comparable in quality to those of the C2 crystal form (fig. S2B). The arrangement of Sec13, Nup145C^{NTD}, Nup84^{NTD}, and the Nup120^{NTD} in the final MR solution is the same as that in the structure of the CNC•sAB-57 complex (fig. S6). The correctness of the solution was confirmed by the calculation of an anomalous difference Fourier map using the phases from the MR solution, which revealed peaks for 20 selenium sites and 1 Os site (fig. S3A-C). Improved phases were obtained with MR-SAD in Phaser using phases from the MR solution and the 21 anomalous scatterers. Subsequent density modification revealed clear tubular density for the triskelion helices, including density for the Nup85^{CTD}, which could be readily docked in the same conformations as observed in the CNC•sAB-57 structure. Additional confirmation of the correctness of the solution was obtained by calculating an anomalous difference Fourier map using anomalous X-ray diffraction data obtained from a CNC•sAB-57•sAB-87 complex crystal derivatized with Ta₆Br₁₄, which revealed 8 tantalum bromide cluster sites (fig. S3A-C).

Of the 20 selenium peaks observed, 11 aligned with the expected selenium sites in the previously determined structures of Nup84^{NTD} and Sec13•Nup145C^{NTD}. An additional 8 selenium peaks were present in the newly built helices of Nup85^{CTD} and Nup145C^{CTD}, which were used to confirm the directionality and approximate sequence assignment of the helices. The final selenium site aligned with the last methionine present in Nup85^{NTD}, but no additional sites were observed for the remainder of the Seh1•Nup85^{NTD} heterodimer (fig. S3A). No additional electron density was visible for Seh1•Nup85^{NTD} in density modified maps either, despite room being available in the lattice to accommodate the molecules (fig. S4B). Thus, this part of the structure is presumed to be disordered in this crystal form.

Structure refinement. Refinement of both structures was performed with heavy restraints using PHENIX, with 1 group B-factor per residue with similarity restraints and positional refinement with secondary structure restraints and reference model restraints for the portions of the structure for which there were high-resolution structures (23). We elected to use models re-refined by the PDB_REDO server, as they had superior geometrical parameters to the previously deposited structures (24). The best strategy for B-factor refinement was determined by comparing the results of test refinements using the following strategies: 1 B-factor per residue with similarity restraints, 2 B-factors per

residue with similarity restraints, 1 B-factor per group, and 1 B-factor per group with TLS parameters (fig. S5A, B). We additionally tested the output of a refinement strategy of 1 B-factor per residue without similarity restraints to ensure that B-factors were meaningfully restrained. Refinement with 1 B-factor per residue with similarity restraints yielded the lowest R-factors and realistic B-factors that were smoothly distributed across the model (fig. S5B). Therefore, we elected to use that strategy with no TLS parameters for the final refinement. The final models of the C2 and P2₁2₁2₁ crystal forms yielded average B factors for the overall model of 716.5 Å² and 536.5 Å², respectively, with comparable B factors for all protein chains (fig. S5D, E). These B-factors include the overall B of the crystal, as is the standard method of reporting B-factors in PHENIX. The resolution limits for both data sets were determined by using the paired refinement technique described by Karplus and Diederichs (25). Paired refinements were performed in 0.2 Å steps from 8.0 Å to 7.0 Å and the resolution limits were selected conservatively before resolution steps that did not improve the model (fig. S5F, G). The final models of the C2 and P2₁2₁2₁ crystal forms, refined to a 7.4-Å and a 7.6-Å resolution, yielded R_{free} and R_{work} values of 35.3 %, 33.0 %, and 34.7 %, 31.8 %, respectively. The stereochemical properties of the two structures were determined by MolProbity (26). The CNC complex structures reported here have similar Ramachandran statistics as the search models used for Sec13•Nup145C^{NTD}•Nup84^{NTD}, Seh1•Nup85^{NTD}, and Nup120^{NTD}. The newly built triskelion has perfect stereochemical parameters with no residues in the disallowed region of the Ramachandran plot. For details of the data collection and refinement statistics see table S2.

Analytical size-exclusion chromatography. Protein-protein interaction experiments were carried out on a Superdex 200 10/300 GL gel filtration column equilibrated in a buffer containing 20 mM TRIS (pH 8.0), 100 mM NaCl, and 5 mM DTT. The various combinations of the yeast CNC components were mixed and incubated for 30 minutes on ice using a 1.2 molar excess of the smaller proteins. Complex formation was monitored by injection of the pre-incubated proteins or the individual components onto the gel filtration column. All proteins were analyzed under identical buffer conditions and complex formation was confirmed by SDS-PAGE of the protein-containing fractions, followed by Coomassie brilliant blue staining.

EM docking. The crystal structure of the yeast CNC was docked into the negative stain EM reconstructions of the yeast complex (EMDB-5151) and the human complex (EMDB-2443) using the Fit in Map function in the UCSF Chimera software package (27).

The crystal structure of the yeast CNC was docked into the cryoelectron EM tomographic reconstruction of the human NPC (EMDB-2444) using an exhaustive, unbiased six-dimensional search using a C α trace of the CNC structure with the program ESSENS from the Uppsala Software Factory package RAVE (28). The rotations were sampled in 10° steps across α , β , and γ for a total of 26,011 rotations, which were each tested at all of the 366,980 grid points which had a map value greater than 1.5. Each combination of rotation and grid point was scored by the K-minimum sum function over the lowest scoring 60 % of the atoms against the average of the 8 nearest grid points, as implemented in ESSENS (28). This exhaustive scoring method produced a clear

separation of 65 top scoring placements from the remaining orientations (fig. S12A). The positioning of the top 65 placements in the EM reconstruction was further refined and rescored using an orthogonal scoring method with the Fit in Map tool of UCSF Chimera (27), which we used to calculate the cross-correlation of the EM map with a simulated map calculated at 34 Å for each docked model (fig. S12B).

Analysis of these solutions and their placements revealed a clear separation between the top 32 solutions and the remainder of solutions. Because of the eight-fold rotational symmetry in the map, unique solutions are each composed of 8 solutions related by rotational symmetry. As a result, the top 32 solutions form four unique rings, all of which are compatible when simultaneously placed into the NPC. The remaining solutions could be classified as one of the following: (1) solutions that refined into one of the above orientations upon refinement, (2) solutions with moderate scores lower than the top scoring 32 orientations and could be discarded due to clashes (fig. S12C), or (3) low scoring solutions that yielded much worse fits than the top 32 solutions upon refinement. Despite the presence of additional features in the map for cytoplasmic filament nucleoporins and associated mRNA export factors, the two CNC rings on the cytoplasmic face and the two CNC rings on the nucleoplasmic face are identical (fig. S12D). This additional unbiased test was taken as final confirmation that this stoichiometry and orientation of CNCs reflects their organization in the NPC.

Illustration and figures. Structural figures were generated using PyMOL (www.pymol.org).

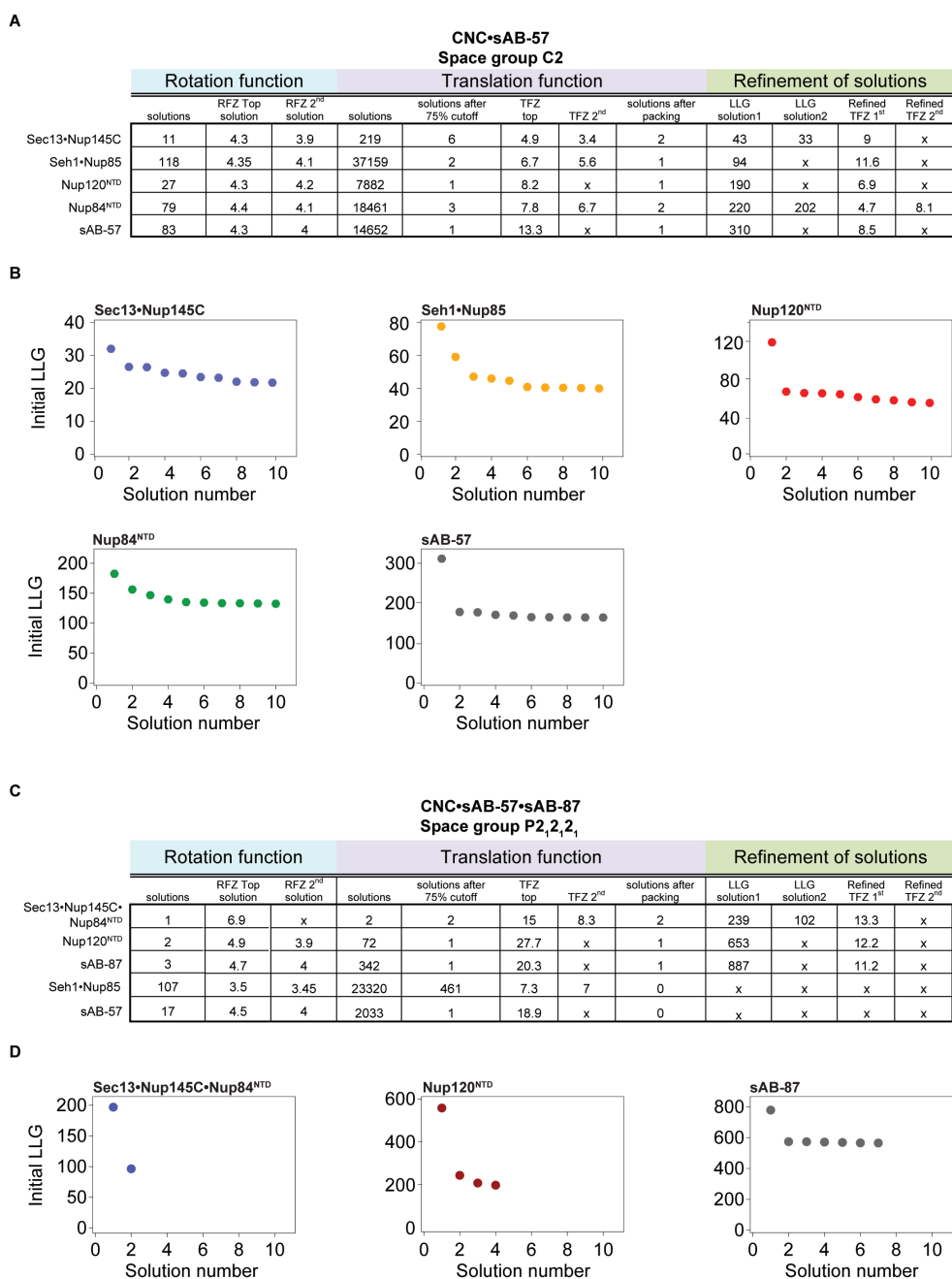


Fig. S1.

Structure determination statistics of the yeast CNC. (A) Table of statistics for each step of molecular replacement performed using Phaser for structure determination of the CNC•sAB-57 complex. Each sequential step was performed with the top solutions from the previous step, and a clear separation of the top solutions was apparent with each step. (B) Plots of the initial log-likelihood gain (LLG) scores for the top 10 peaks from the translation function step of Phaser for structure determination of the CNC•sAB-57 complex. (C) Table of statistics for each step of molecular replacement performed using

Phaser for structure determination of the CNC•sAB-57•sAB-87 complex. Each sequential step was performed with the top solutions from the previous step, and a clear separation of the top solutions was apparent with each step. **(D)** Plots of the initial log-likelihood gain (LLG) scores for the top peaks from the translation function step of Phaser for structure determination of the CNC•sAB-57•sAB-87 complex. For each step, there were only a handful of peaks selected from the rotation function, resulting in fewer peaks in the translation function.

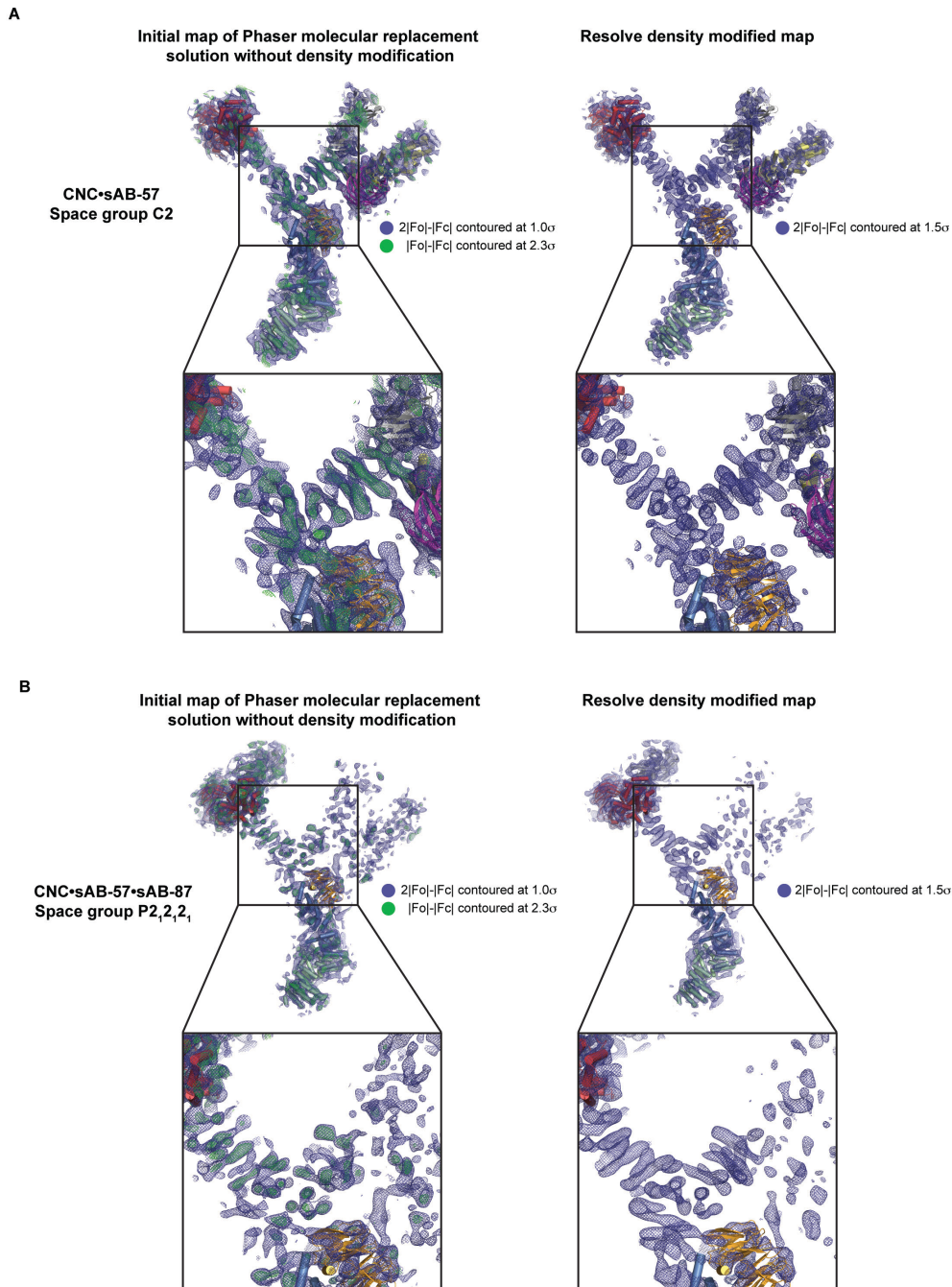


Fig. S2

Electron density during structure determination of the yeast CNC. The electron density for the initial molecular replacement and after density modification for the crystal structures of the (A) CNC•sAB-57 and (B) CNC•sAB-57•sAB-87 complexes are shown. Clear density was visible for the triskelion helices after successful placement of previously solved crystal structures (left) and remained after density modification (right), which was performed prior to model building. The models visualized are the direct output from molecular replacement prior to any interpretation.

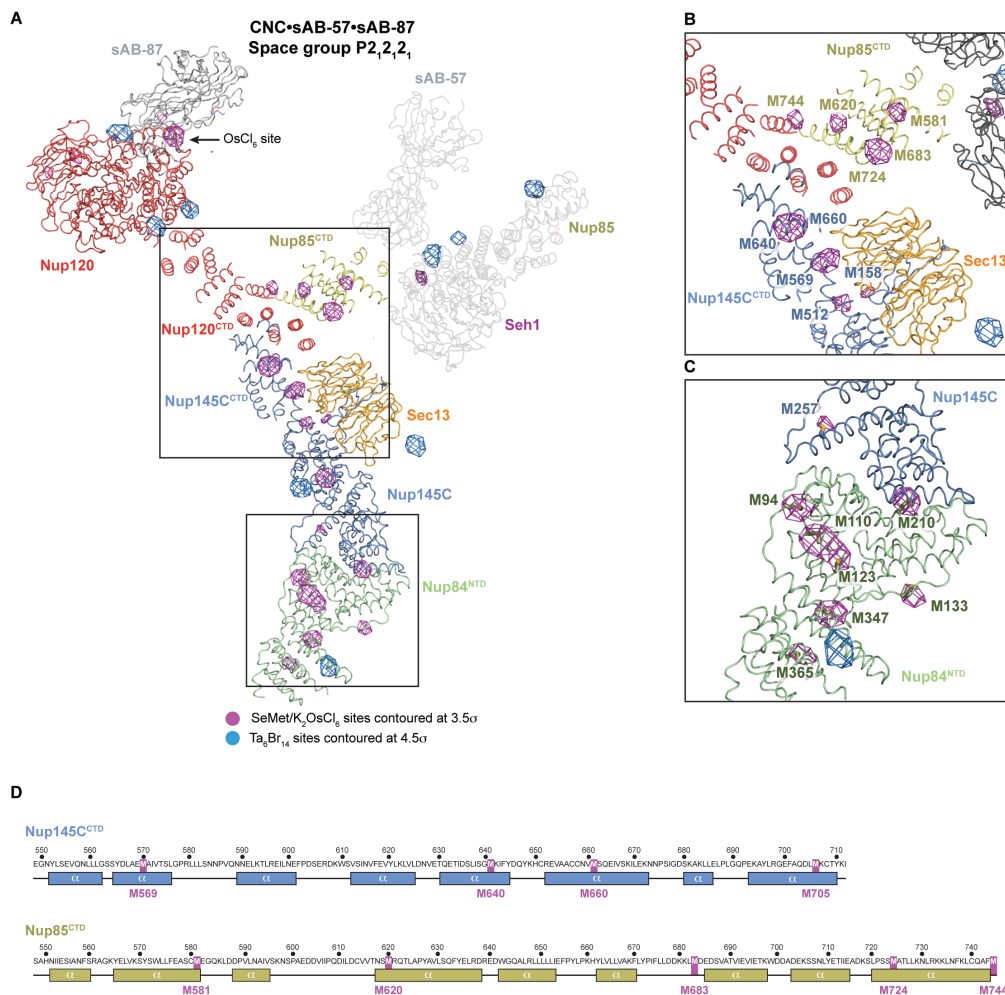


Fig. S3.

Location of anomalous scatterers in crystals of the CNC•sAB-57•sAB-87 complex.

Anomalous difference Fourier maps were calculated for X-ray diffraction data collected at the selenium and tantalum peak wavelengths for CNC•sAB-57•sAB-87 crystals grown with SeMet labeled protein and soaked with K₂OsCl₆ or native CNC•sAB-57•sAB-87 crystals soaked with tantalum bromide clusters (Ta₆Br₁₄). (A) A ribbon representation of the structure of the CNC•sAB-57•sAB-87 complex, with the anomalous difference Fourier maps of X-ray diffraction data collected at the selenium (purple) or tantalum (blue) peak wavelengths contoured at 3.5 σ and 4.5 σ, respectively. Tantalum peaks adjacent to Nup85^{NTD} and a peak corresponding to the last selenium site in Nup85^{NTD} are visible despite the molecule being disordered in the crystal. (B) Close-up view of selenium sites present for the triskelion helices for which there are no high-resolution structures. 8 peaks are visible and confirm the positioning and orientation and approximate sequence assignment in the structure. (C) Close-up view of the selenium peaks in Nup84^{NTD} and Nup145C, with stick representations of the SeMet residues highlighting the expected sites. (D) Sequence and secondary structure prediction of Nup145C^{CTD} and Nup85^{CTD} with methionine residues highlighted.

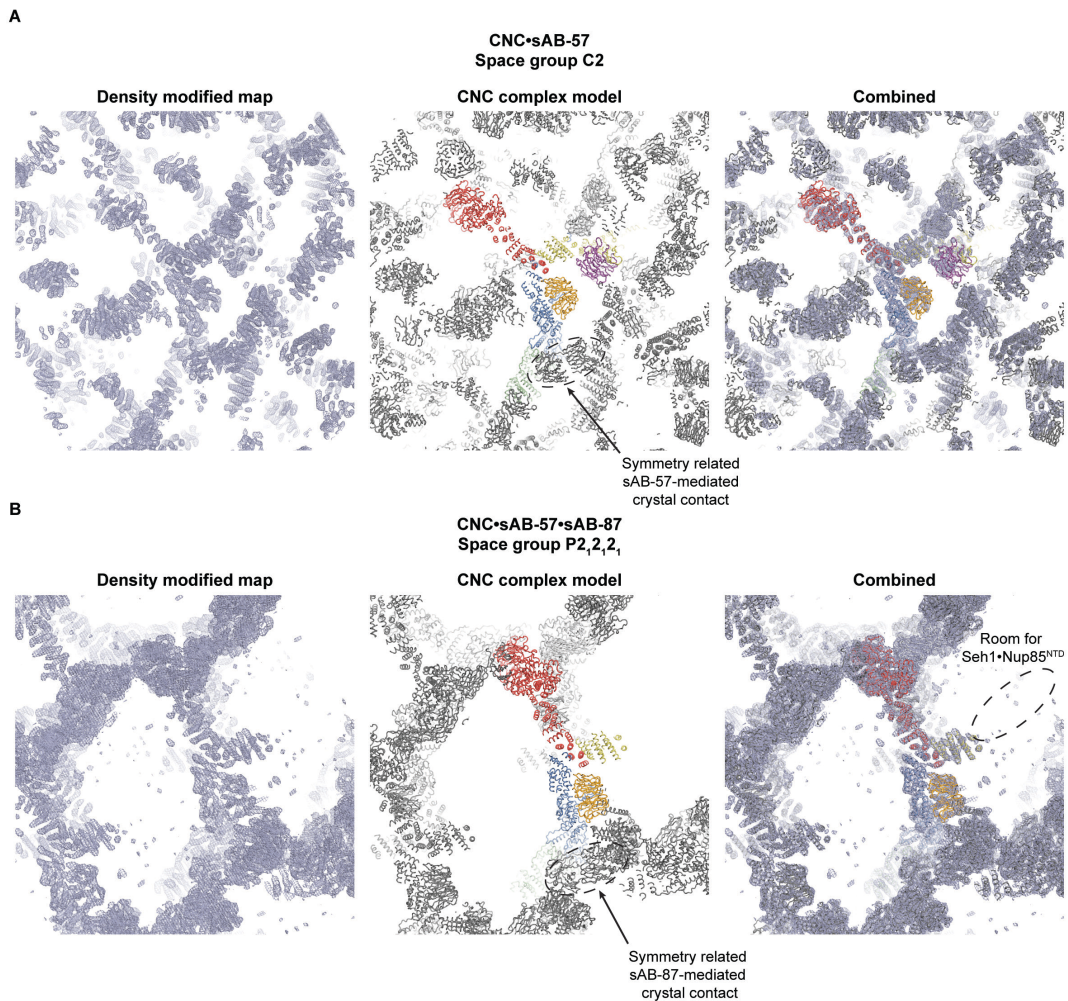


Fig. S4.

Crystal packing in crystals of CNC•sAB-57 and CNC•sAB-57•sAB-87. Representative views of the crystal packing for crystals of the CNC•sAB-57 complex (**A**) and CNC•sAB-57•sAB-87 complex (**B**). (left) Uncarved density-modified electron density contoured at 1σ demonstrates the large solvent channels present in both crystals. (center) Ribbon representation of the asymmetric unit and surrounding symmetry mates colored gray highlights a major crystal contact made in both crystals by a synthetic antibody with the Nup145C•Nup84^{NTD} interface. (right) Combined view of both the electron density and unit cell.

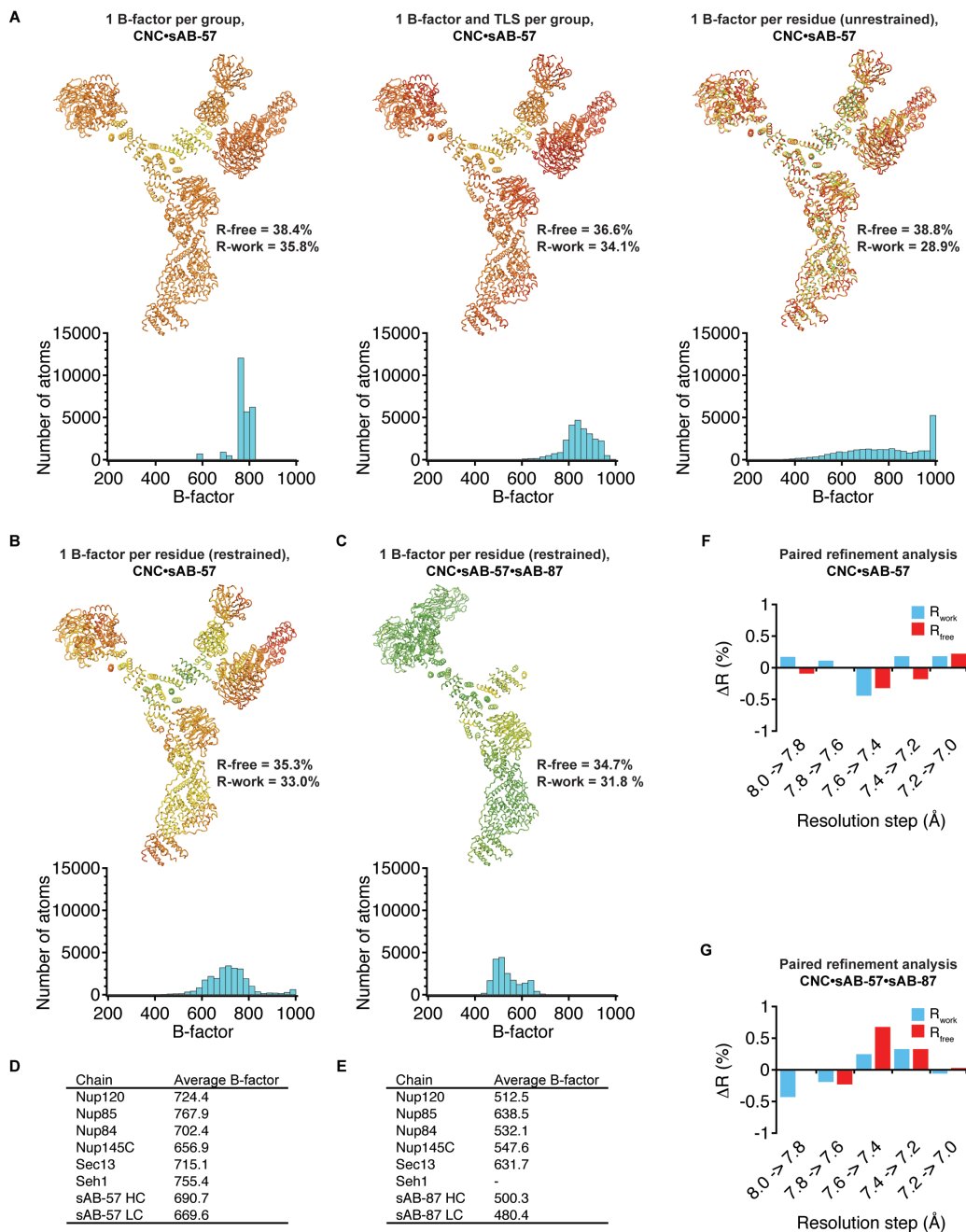


Fig. S5.

Determination of optimal refinement strategy, resolution limits, and B-factor analysis. (A) Ribbon representations of the CNC•sAB-57 complex colored from blue to red by B-factor for various alternative refinement strategies with histograms of the B-factor distribution below. (B) Ribbon representation of the CNC•sAB-57 complex refined with the final refinement strategy of 1 B-factor per residue and colored on the same scale as in (A). (C) Ribbon representation of the CNC•sAB-57•sAB-87 complex refined with 1 B-factor per residue and colored on the same scale as in (A). (D-E) Average B-factors per protein chain for the CNC•sAB-57 complex (D) or CNC•sAB-57•sAB-87 complex (E).

(F-G). Paired refinement analysis of the resolution limit as described by Karplus and Diederichs (25) for the **(F)** CNC•sAB-57 complex or **(G)** CNC•sAB-57•sAB-87 complex. The improvement in R-factors gained for each 0.2 Å shell of data was assessed by re-calculating the R-factors in the lower resolution data after refinement with the higher resolution data.

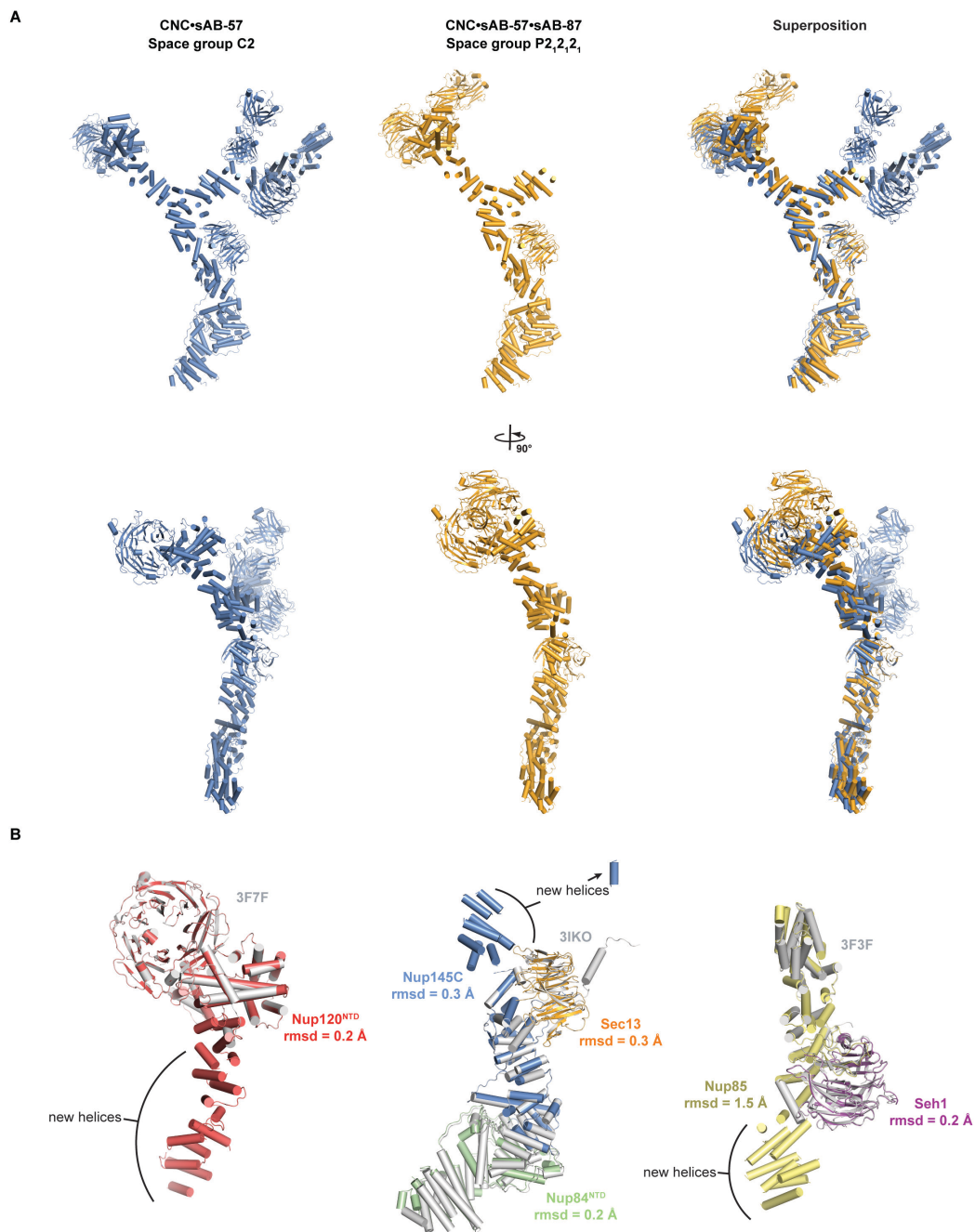


Fig. S6.

Comparison of the yeast CNC structures from different crystal forms. (A) The structures of the CNC•sAB-57 complex (blue) and CNC•sAB-57•sAB-87 complex (orange) are shown alone and superimposed over the central Sec13•Nup145C core. A view rotated by 90° is shown below. (B) Superposition of previously determined structures of the Nup120^{NTD}, the Sec13•Nup145C•Nup84^{NTD} hetero-trimer and the Seh1•Nup85 pair used for molecular replacement (PDB ID 3F7F, 3IKO, and 3F3F) (6, 8,

9) with their counterparts from the final crystallographic model. Cartoon representations are colored as in [Fig. 1](#), whereas previous structures are colored in gray. Calculated root mean square displacements (rmsds) are indicated for each molecule. Nup85 has a large rmsd due to a large kink in the helical solenoid. Notably, crystal packing interactions of sAB-87 induce a slight rotation of the central triskelion.

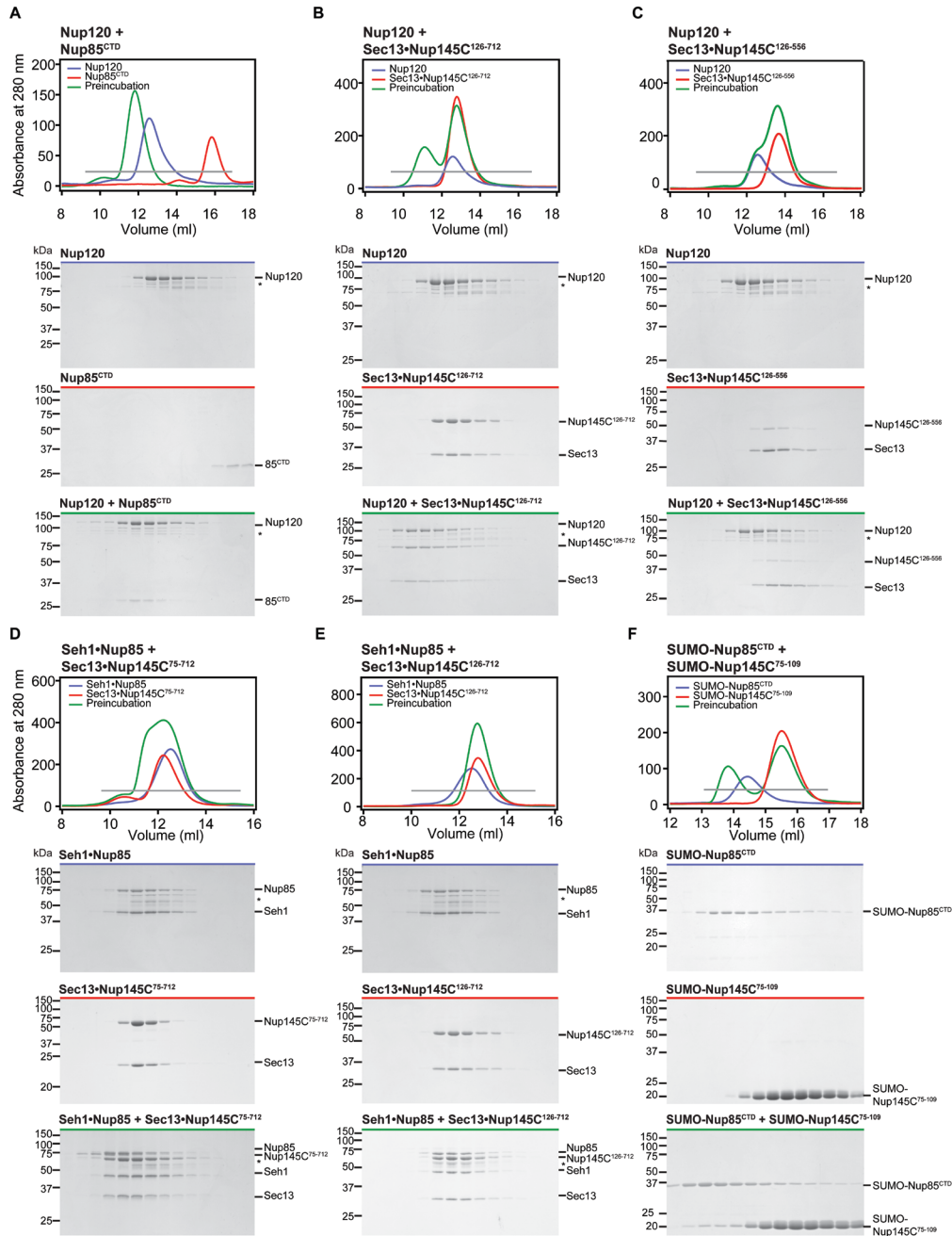


Fig. S7.

Biochemical characterization of the yeast CNC triskelion. (A-C) Nup120 interactions. Gel filtration profiles for Nup120 (A-C, blue), Nup85^{CTD} (A, red), Sec13•Nup145C¹²⁶⁻⁷¹² (B, red) and Sec13•Nup145C¹²⁶⁻⁵⁵⁶ (C, red) and after pre-incubation (green). (D-E) Seh1•Nup85 interactions. Gel filtration profiles for Seh1•Nup85 (D-E, blue), Sec13•Nup145C⁷⁵⁻⁷¹² (D, red), Sec13•Nup145C¹²⁶⁻⁷¹² (E, red) and after pre-incubation (green). (F) Interaction analysis between Nup85^{CTD} and Nup145C. Gel filtration profiles for SUMO-Nup85^{CTD} (blue) and SUMO-Nup145C⁷⁵⁻¹⁰⁹ alone (red) and after pre-incubation (green). Gray bars in the gel filtration profiles indicate the fractions resolved

on the SDS-PAGE gels. Molecular mass standards and the positions of the proteins are indicated. Asterisks indicate degradation products. SDS-PAGE gels were stained with Coomassie brilliant blue. This size exclusion chromatography data is in agreement with previously published mass spectrometry data, which reported cross-links between Nup120^{K972} and Nup145C^{K672,K681,K694}, Nup120^{K943} and Nup145C^{K681}, and Nup120^{K972} and Nup85^{K772,K733,K734} (12).

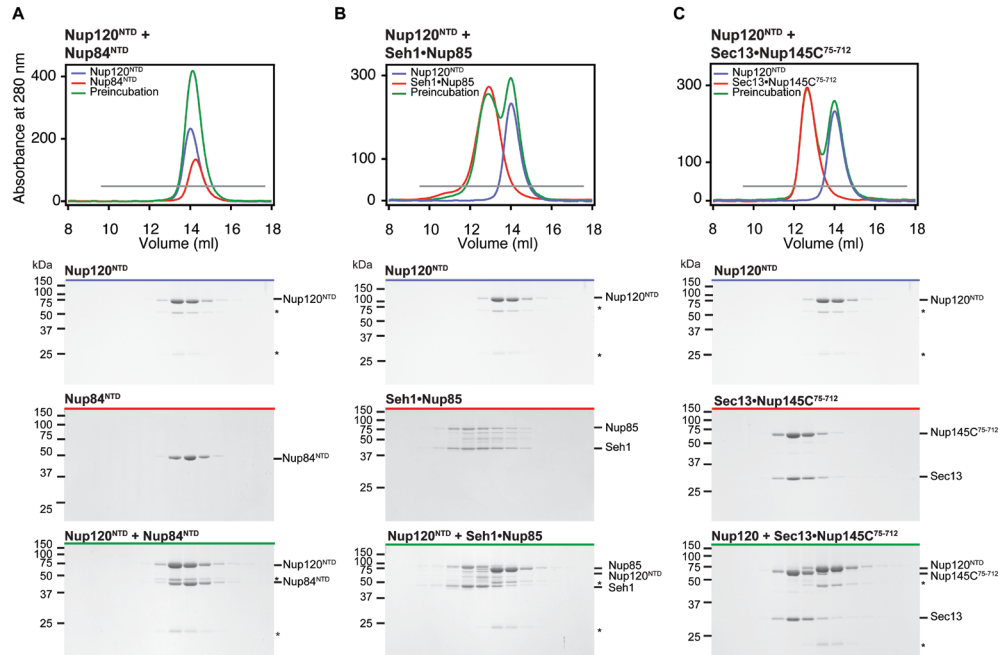


Fig. S8. Nup120^{NTD} forms no interactions with Nup84^{NTD}, Seh1•Nup85, or Sec13•Nup145C⁷⁵⁻⁷¹². (A-C) Gel filtration profiles for the proteins alone: Nup120^{NTD} (A-C, blue), Nup84^{NTD} (A, red), Seh1•Nup85 (B, red) and Sec13•Nup145C⁷⁵⁻⁷¹² (C, red) and after pre-incubation of the different complexes (green). Gray bars in the gel filtration profiles indicate the fractions resolved on the SDS-PAGE gels. Molecular mass standards and the positions of the proteins are indicated. Asterisks indicate degradation products. SDS-PAGE gels were stained with Coomassie brilliant blue.

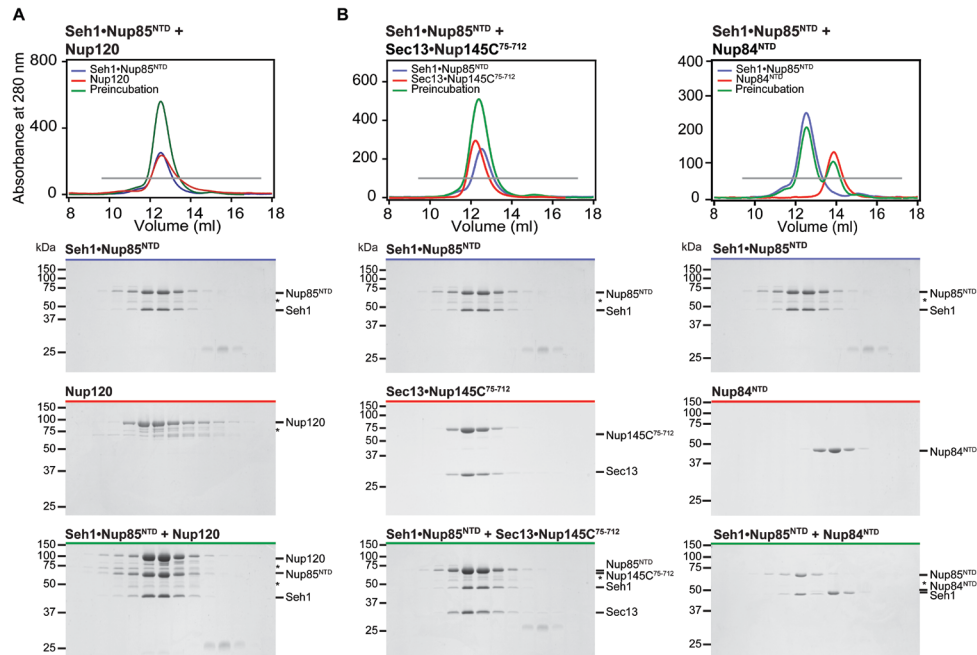


Fig. S9.

Seh1•Nup85^{NTD} forms no interactions with Nup84^{NTD}, Nup120 or Sec13•Nup145C⁷⁵⁻⁷¹². (A-C) Gel filtration profiles of Seh1•Nup85^{NTD} (A-C, blue), Nup120 (A, red), Sec13•Nup145C⁷⁵⁻⁷¹² (B, red), Nup84^{NTD} (C, red) and after pre-incubation (green). Gray bars in the gel filtration profiles indicate the fractions resolved on the SDS-PAGE gels. Molecular mass standards and the positions of the proteins are indicated. Asterisks indicate degradation products. SDS-PAGE gels were stained with Coomassie brilliant blue.

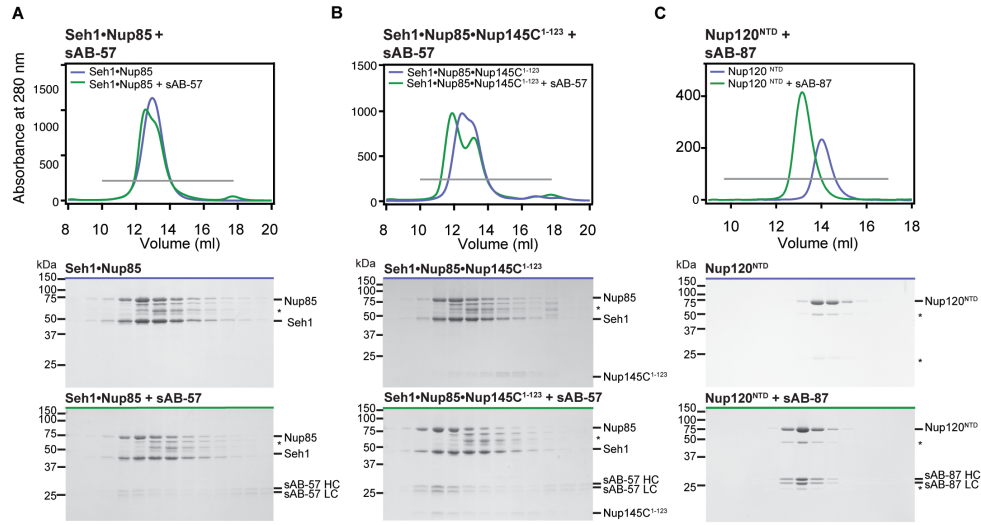


Fig. S10.

Synthetic antibody (sAB) interactions. (A) sAB-57 interacts with Seh1•Nup85. Gel filtration profiles for Seh1•Nup85 (blue), Seh1•Nup85 preincubated with sAB-57 (green). (B) sAB-57 interacts with Seh1•Nup85•Nup145C¹⁻¹²³. Gel filtration profiles for Seh1•Nup85•Nup145C¹⁻¹²³ (blue), Seh1•Nup85•Nup145C¹⁻¹²³ preincubated with sAB-57 (green). Although sAB-57 can weakly interact with Seh1•Nup85 (A), the interaction is only stoichiometric in the presence of Nup145C¹⁻¹²³ (B). (C) sAB-87 interacts with Nup120^{NTD}. Gel filtration profiles for Nup120^{NTD} (blue) and Nup120^{NTD} pre-incubated with sAB-87 (green). Notably, sAB-57 and sAB-87 non-specifically interact with the Superdex 200 resin in the tested buffer conditions and were thus not analyzed in isolation. Gray bars in the gel filtration profiles indicate the fractions resolved on the SDS-PAGE gels. Molecular mass standards and the positions of the proteins are indicated. Asterisks indicate degradation products. SDS-PAGE gels were stained with Coomassie brilliant blue.

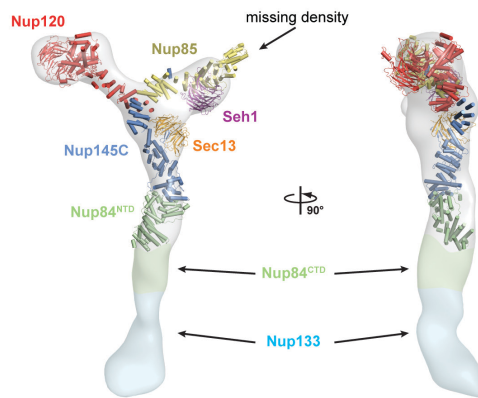


Fig. S11.

Comparison of the yeast CNC crystal structure and its negative-stain EM reconstruction. Two views of the crystal structure, colored as in Fig. 1, superimposed on the negative-stain EM reconstruction (EMDB-5151 (4)) shown as a gray surface. Portions of the EM reconstruction are shaded green or cyan to indicate components of the complex that were not crystallized.

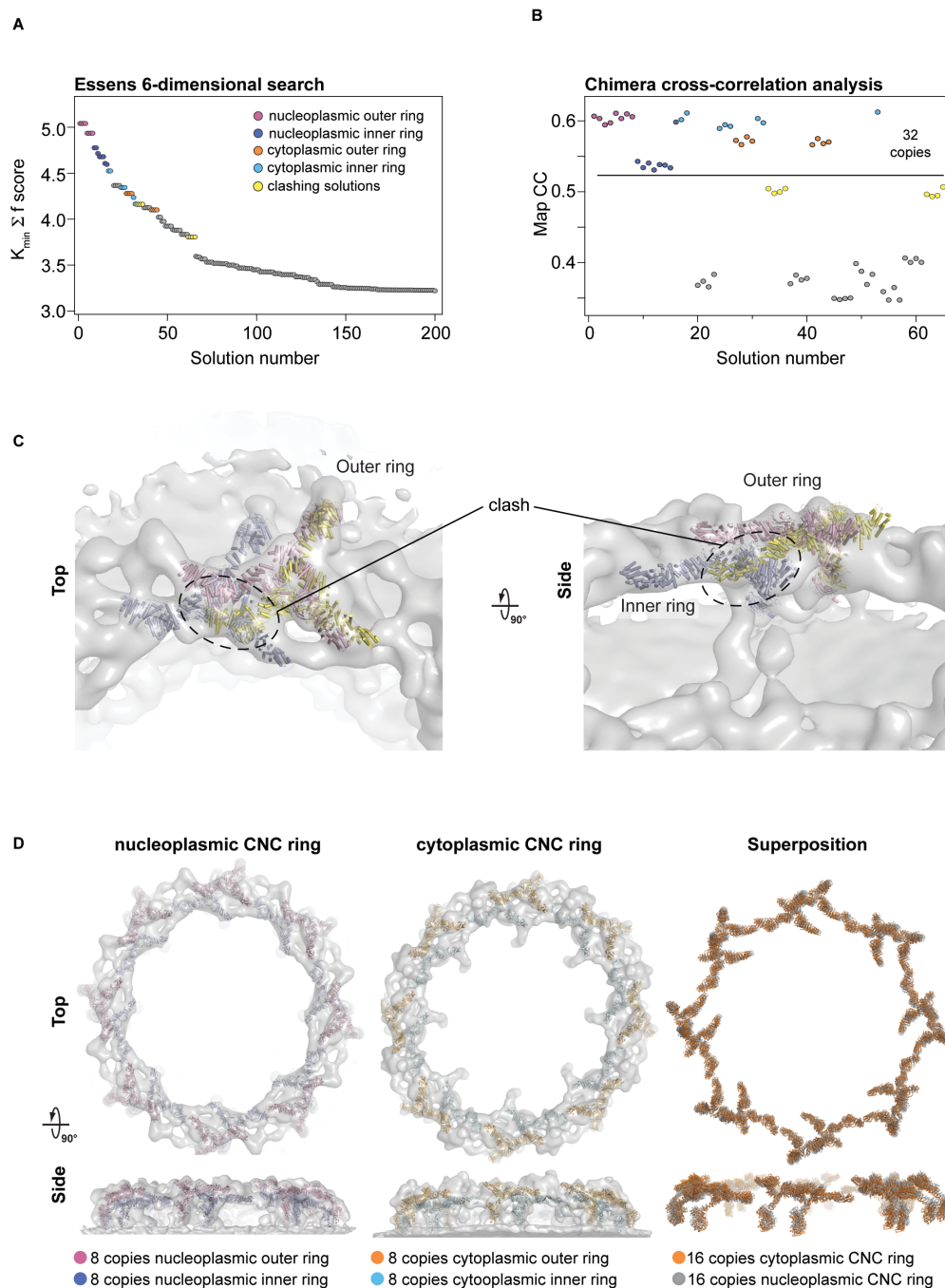


Fig. S12.

EM docking statistics. (A) The top 200 solutions (out of several thousands) plotted by ranked solution number and score. Top scoring solutions after refinement and rescoring with UCSF Chimera Fit in Map analysis are highlighted. (B) The top 65 solutions which showed a clear separation from the remaining solutions were refined and rescored with the UCSF Chimera Fit in Map tool. The highest 32 scoring solutions could be separated into four groups related by eight-fold rotational symmetry and are colored accordingly. The next highest scoring group of solutions, which clash with the top 32 solutions, is

colored in yellow. **(C)** Analysis of the next highest group of solutions. A member from each of the top scoring group of solutions is shown in cartoon representation, colored as in (A). The third solution clashes with the top two solutions, which are compatible with one another. **(D)** Comparison of the nucleoplasmic and cytoplasmic rings. Top and side views for the two faces of the NPC are shown with the members of each ring docked into the EM envelope. A superposition of the two rings without the EM density is shown on the right, which highlights the identical arrangement of CNCs despite no *a priori* information in the map restricting them to be the same.

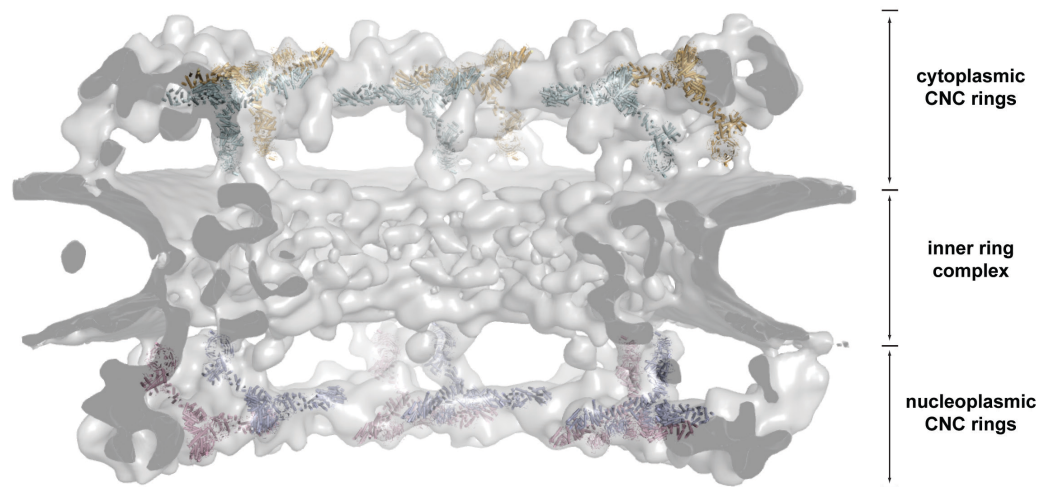


Fig. S13.

EM docking. A side view of the NPC is shown from within the central channel, highlighting the placement of 32 CNCs to the nuclear and cytoplasmic densities in the cryo-electron tomography reconstruction of the human NPC. The subunit organization of the inner ring remains unknown.

Table S1.**Bacterial expression constructs**

Protein	Residues	Expression vector	Restriction sites	N-terminal overhang	C-terminal overhang	Reference
Nup120 ^{♦,‡}	1-1037	pET8c	NdeI, NotI	MGSSHHHHHHSD	None	Lutzmann et al.
Nup145C	75-712	pETDuet1	BamHI, NotI	MGSSHHHHHHHSQDP	None	This work
Sec13 ^{♦,‡}	1-297		NdeI, XhoI	None	None	
Nup145C	75-556	pETDuet1	BamHI, NotI	MGSSHHHHHHHSQDP	None	This work
Sec13	1-297		NdeI, XhoI	None	None	
Nup145C	126-712	pETDuet1	BamHI, NotI	MGSSHHHHHHHSQDP	None	This work
Sec13	1-297		NdeI, XhoI	None	None	
Nup145C ^{NTD}	126-556	pETDuet1	BamHI, NotI	MGSSHHHHHHHSQDP	None	Nagy et al.
Sec13	1-297		NdeI, XhoI	None	None	
Nup85	44-744	pETDuet1	NdeI, NotI	MGSSHHHHHHHSQDP	None	This work
Seh1 ^{♦,‡}	1-349		NheI, XhoI	None	None	
Nup85 ^{NTD}	1-570	pETDuet1	NdeI, NotI	MGSSHHHHHHHSQDP	None	Debler et al.
Seh1	1-349		NheI, XhoI	None	None	
Nup85 ^{CTD}	533-744	pET-MCN-SUMO	BamHI, NotI	S	None	This work
Nup84 ^{NTD♦}	1-451	pET28a-PreS	NdeI, NotI	GPH	None	This work
Nup84 ^{NTD‡}	1-451	pET28a-PreS-avi	NdeI, NotI	MGSSHHHHHHSSGLEVL FQGPLMSGLNDIFEAQKI EWHEGSAGGSGHM	None	This work
Nup145C	75-109	pET-MCN-SUMO	BamHI, NotI	S	None	This work
Nup145C	1-123	pET28a-SUMO	BamHI, NotI	S	None	This work
Nup120 ^{NTD‡}	1-721	pGEX-4T1-TEV	BamHI, NotI	GAMGS	None	Seo et al.
Nup120 ^{NTD‡}	1-721	pGEX-4T1-TEV-avi	BamHI, NotI	GAMGSSGLNDIFEAQKIE WHEGSAGGSGGS	None	This work
sAB-57 LC	1-217	pSFV4	NcoI, SalI	None	VDKKVEPKSCDKT HTGGSHHHHHH	This work
sAB-57 HC [♦]	1-271					
sAB-87 LC	1-217	pSFV4	NcoI, SalI	None	VDKKVEPKSCDKT HTGGSHHHHHH	This work
sAB-87 HC [♦]	1-267					

[♦] Constructs that were used for crystallization of the coat nucleoporin complex

[‡] Constructs that were used for sAB selection

Table S2.

Crystallographic analysis

	Yeast CNC•sAB-57	<i>SeMet/K₂O_sCl₆</i> Yeast CNC•sAB-57•sAB-87	<i>Ta₆Br₁₂</i> Yeast CNC•sAB-57•sAB-87
Data collection			
Protein	Yeast CNC•sAB-57	Yeast CNC•sAB-57•sAB-87	Yeast CNC•sAB-57•sAB-87
Synchrotron	APS ^a	APS ^a	APS ^a
Beamline	23-ID-D	23-ID-D	23-ID-D
Space group	C2	P2 ₁ 2 ₁ 2 ₁	P2 ₁ 2 ₁ 2 ₁
Cell dimensions			
<i>a</i> , <i>b</i> , <i>c</i> (Å)	211.2, 186.4, 199.8	117.1, 180.0, 441.2	113.0, 175.8, 442.6
α , β , γ (°)	90.0, 100.9, 90.0	90.0, 90.0, 90.0	90.0, 90.0, 90.0
Wavelength	0.9794	0.9794	1.2548
Resolution (Å)	70.0 – 7.4	50.0 – 7.6	50.0 – 10.4
<i>R</i> _{meas} (%) ^b	10.1 (212.5)	10.8 (121.4)	14.9 (134.7)
<i>CC</i> _{1/2}	99.9 (51.8)	99.9 (60.6)	99.7 (80.3)
$\langle I / \sigma I \rangle$ ^b	15.3 (1.4)	13.5 (1.8)	6.4 (1.6)
Completeness (%) ^b	99.0 (94.9)	99.2 (97.7)	99.0 (100.0)
No. of observations	139,658	167,573	45,583
No. of unique reflections ^b	10,375 (1,578)	22,082 (3,431)	8,095 (1,062)
Redundancy ^a	13.5 (13.5)	7.0 (7.0)	5.6 (5.7)
Refinement			
Resolution (Å)	70.0 – 7.4	50.0 – 7.6	
No. of reflections	10,227	22,065	
No. of reflections test set	1,022 (10.0 %)	2,193 (9.9 %)	
<i>R</i> _{work} / <i>R</i> _{free}	33.0 / 35.3	31.8 / 34.7	
No. Protein atoms	26,147	19,824	
R.m.s deviations			
Bond lengths (Å)	0.006	0.005	
Bond angles (°)	1.2	1.1	
<i>B</i> -factors ^c	716.5	536.5	
Ramachandran plot ^d			
Favored (%)	91.0	91.9	
Additionally allowed (%)	7.3	6.4	
Outliers (%)	1.7	1.8	

^aAPS, Advanced Photon Source^bHighest-resolution shell is shown in parentheses^cB-factors include overall B-factor of the crystal^dAs determined by MolProbity (26)

Movie S1.

Rotating structure of the yeast CNC in cartoon representation. The yeast CNC is colored according to [Fig. 1](#).

Movie S2.

Rotating structure of the yeast CNC docked into the negative-stain EM reconstruction of the yeast CNC. The envelope of the EM reconstruction is shown in gray and the yeast CNC is colored according to [Fig. 1](#).

Movie S3.

Rotating structure of the yeast CNC docked into the negative-stain EM reconstruction of the human CNC. The envelope of the EM reconstruction is shown in gray and the yeast CNC is colored according to [Fig. 1](#).

Movie S4.

Architecture of the nuclear pore complex coat. Details as discussed in the text. The movie starts with an orientation of the NPC in the same orientation as in [Fig. 4A](#).